

Generation and control of high-order harmonics by the interaction of an infrared laser with a thin graphite layer

Ashish Kumar Gupta, Ofir E. Alon,* and Nimrod Moiseyev

Department of Chemistry and Minerva center for Nonlinear Physics of Complex Systems, Technion-Israel Institute of Technology, Haifa 32000, Israel

(Received 27 February 2003; revised manuscript received 19 May 2003)

We demonstrate the possibility to control the generation of high-order harmonics by a thin layer of graphite upon varying the polarization and intensity of the laser field. While for monochromatic linearly polarized laser fields all odd-order harmonics are emitted, we find that even for very large deviations from exact circular polarization (the elliptical polarization angle is $\theta=45^\circ$), the dynamical symmetry based selection rules $\Omega = (6m \pm 1)\omega$, $m=1,2,3 \dots$, where ω and Ω are the fundamental and harmonic frequencies [Phys. Rev. Lett **80**, 3743, 1998], are valid. Our results show that the generation and control of high-order harmonics in thin layers of graphite by varying the polarization and intensity of an infrared laser field is feasible and should be observed in experiments.

DOI: 10.1103/PhysRevB.68.1651XX

PACS number(s): 42.65.Ky, 42.50.Hz, 03.65.-w, 31.15.Hz

I. INTRODUCTION

High-order harmonic generation (HHG) in atomic gases has been extensively studied both experimentally and theoretically in the past 20 years (see, e.g., Ref. 1 and references therein). Nowadays, such a table-top source of coherent short-wavelength radiation has found various (scientific) applications as a probing and diagnostic tool in studying ultrafast physical processes (see, e.g., Refs. 2–5). A common characteristic of HHG-based radiation sources is their multichromaticity. To be specific, irradiating gases by *monochromatic* linearly/elliptically-polarized laser fields leads to the emission of all, and only, odd harmonics up to a certain cutoff. This selection rule (SR), as is well known, is easily explained by the combined *spherical* symmetry of atoms and the monochromaticity of the laser field, both within (see, e.g., Ref. 6) and beyond⁷ perturbation theory. Of course, it would become very practical to have an almost monochromatic, HHG-based, source of coherent short-wavelength radiation.

Recently, it has been shown that discrete spatial symmetries, e.g., rotations in molecules^{8–12} (and in thin crystals⁸) and screw axes in nanotubes,¹³ when combined with circularly polarized (monochromatic) laser fields, can lead to high-order dynamical symmetries (DSs) and, as a result, to a much more selective HHG by such target systems. Specifically, given a discrete symmetry of order N and a (monochromatic) circularly-polarized field, the corresponding SR's for the HHG spectra (HHGS) are given by the relation $lN \pm 1, l=1,2,3, \dots$. Notwithstanding, a central point in the prediction of these unusual SRs is the requirement that the target-system should be aligned in the (circularly polarized) laser field.^{8,13}

To achieve a better-than-random degree of orientation in the gas phase, one possibility is to try and prealign molecules, say of benzene (six fold rotational symmetry), using a first laser pulse, and, meanwhile, applying a second—much shorter—pulse to generate the selective high-order harmonics (see Ref. 14 in this context). This solution is quite com-

plicated technically, since it is hard to align the molecules to an angle with an accuracy which is smaller than $\pm 5^\circ$. The difficulties arising when one wishes to align molecules in the gas phase are avoided if one employs a solid surface, and in particular a crystalline (spatially periodic) target. As mentioned above, it has been shown that aligned single-walled carbon nanotubes are excellent candidates for the selective and efficient generation of HOHs.¹³ However, the present technology of carbon-nanotube manufacturing cannot yet achieve a *well-aligned* sample of *uniform* chirality, a prerequisite for the selective generation of HOHs by such a target system.¹³ In view of this, a thin crystalline layer seems to be a good and *practical* candidate for the first experimental demonstration of HHG governed by the DS-based SRs put forward in Ref. 8.

HHG from solid metallic *surfaces* has been demonstrated by several groups (see, e.g., Refs. 15–18). However, in such a type of experiments *all* even and odd harmonics up to a certain cutoff are observed since there is no SR for HHG processes at surfaces for a general incident angle. Moreover, the usage of higher laser intensities ($I_0 > 10^{16}$) and longer pulse durations (of the order of picoseconds) creates a plasma at the surface (where the HOHs are generated), i.e., a severe and nonreversible damage accompanies such experiments. The approach we follow in this work (also see Refs. 19 and 20) is to employ moderate field intensities that, upon passing through a thin crystalline film and taking advantage of the crystal's *bulk* spatially periodic potential, induce a reversible nonlinear optical response leading to HHG processes. In other words, the experiment we propose is a generalization to the nonperturbative regime of the common methods of producing second and third harmonics through the interaction of a monochromatic laser field with crystals. In this context, the recent experiments of fourth-harmonic generation at crystalline surfaces, that moreover was used to resolve their symmetry at peak intensity as low as $2\text{--}5 \times 10^{11}$ W/cm² (Ref. 21) and the measurements of third-harmonic generation in multiwalled carbon nanotubes, revealing an unusual non-perturbative behavior already for

$I_0 \sim 10^{10}$ W/cm² (Ref. 22) are good examples of such *reversible* (i.e., nondestructive) nonlinear dynamics. In view of the above, in the present work we have selected a crystalline target system possessing the highest-possible (sixfold) discrete symmetry, graphite to be specific, to design a practical experiment aiming at demonstrating the DS-based SRs for the HHGS put forward in Ref. 8. As is well known, the (unbuckled) structure of bulk graphite possesses S_6 screw and S_6 rotation-reflection axes; a thin film of (unbuckled) graphite possesses the S_6 rotation-reflection axes (for an even number of graphene layers); and graphene [the two-dimensional (2D) monolayer of graphite] possesses the C_6 rotation axes. In order to simplify the calculations, we restrict ourselves to studying the non-linear response of graphene, assuming that for thin graphite films the much weaker interlayer interaction would not change significantly the HHGS obtained by the monolayer.

The limitations on the intensity of the incident radiation and the width of the graphite films are dictated as follows. Recently, Lenzner *et al.*²³ observed that multiphoton ionization rates for silica are substantially lower than those predicted by the Keldysh theory for sub-10-fs laser pulses and intensities in excess of 10^{14} W/cm², slightly below damage threshold. By doing so, the authors of Ref. 23 suggested “to explore an entirely new—nonperturbative—regime of reversible nonlinear optics in solids” (in excess of 10^{14} W/cm²). Also, recent theoretical studies²⁴ for the ultrafast laser ablation of a graphite film with a 20-fs laser pulse of 620-nm wavelength have revealed two damage mechanisms, evolving on a time scale of a few tens of femtoseconds, starting at thresholds (for the above parameters) of about $I_0 \approx 8.5 \times 10^{12}$ W/cm² and $I_0 \approx 1.45 \times 10^{13}$ W/cm². Combining the above data and focusing on short infrared (IR) laser pulses we, thus, take a damage threshold of about 10^{13} W/cm² for a thin graphite film. Of course, the target should be sufficiently thin to allow for the fundamental and harmonics to propagate through and exit the crystal. Accordingly (also see Ref. 20), we consider thin graphite films, the thickness of which is of the order of 10 nm, i.e., thin films composed of a few tens of graphene monolayers.

There have been several approaches to describe and compute HHGS from solids and spatially-periodic structures (crystals or superlattices), see, e.g., Refs. 19,20 and 25–29. For crystals, one should take into account the delocalization of the electrons, being extended in Bloch-type orbitals rather than localized in atomic-or molecular-type orbitals. Accordingly, we employ a nonrelativistic quantum-mechanical microscopic theory of HHG from spatially periodic structures which describes the modified energy bands (EBs) [so called quasienergy bands (QEBs)] of the crystalline sample.^{20,26} The bare monolayer of graphene is described within the tight binding (TB) method with four orbitals ($2s, 2p_x, 2p_y$, and $2p_z$) per carbon.³⁰ Accordingly, to describe the interaction of graphene with the time-periodic laser field and the resulting generation of HOHs, we develop a Floquet TB (FTB) approach that generalizes the method applied to compute HHGS from 1D superlattices^{27,26} and single-walled carbon nanotubes.¹³ The methodology in our FTB approach is that the TB-based interaction term is represented in the momen-

tum gauge of the electro(magnetic) field and is constructed from basis functions (orbitals) in real space. In this way the TB-based *time-dependent* Hamiltonian preserves the lattice translational symmetry, and QEBs could be defined and calculated. As is demonstrated and detailed below, we find that selective HHGSs should be observed while irradiating a thin graphite film with infrared IR monochromatic circularly polarized fields well below its (first) damage threshold.

The structure of the paper goes as follows. In Sec. II we present the methodology of the theory and calculations, namely, the choice of symmetry-adapted basis set, and the calculation of the HHGS resulting from electrons driven in a spatially periodic material. In Sec. III we present and discuss our results. A brief summary is given in Sec. IV. Finally, the Floquet Hamiltonian matrix elements and numerical values of relevant integrals are respectively depicted in Appendixes A and B.

II. FORMULATION AND METHODOLOGY

A. Symmetry adapted unit cell of graphene

Graphene has a C_6 rotation axis and there are different possibilities to define the primitive unit cell. However, aiming at studying the DS-based effects resulting while the solid surface interacts with a laser field, we do not chose the *smallest* possible two-atom unit cell of graphene.³⁰ Rather, we chose the symmetry-adapted six-atom unit cell shown in Fig. 1(a) which is the smallest unit cell possessing the C_6 symmetry, having in mind the employment of the TB approach. Accordingly, the smaller first Brillouin zone (BZ) is obtained [see Fig. 1(b)]. $\vec{a}_1 = [(3\sqrt{3}/2)b, \frac{3}{2}b]$ and $\vec{a}_2 = [(3\sqrt{3}/2)b, -\frac{3}{2}b]$ are the corresponding unit vectors, where b is the bond length between two adjacent carbon atoms. Note that the unit vectors are $\sqrt{3}$ times longer than the conventional ones, and hence the unit-cell area is three times larger than that of the conventional two-atom one.³⁰ The first BZ is the area bounded by the thick hexagon [see Fig. 1(b)]. $\vec{b}_1 = (2\pi/3\sqrt{3}b, 2\pi/3b)$ and $\vec{b}_2 = (2\pi/3\sqrt{3}b, -2\pi/3b)$ are the corresponding unit vectors in the reciprocal lattice. Note that the unit vectors in reciprocal space are $\sqrt{3}$ times shorter than the conventional ones, and hence the area of the first BZ is 1/3 than that of the conventional two-atom one.³⁰ Of course, the choice of the larger symmetry-adapted unit cell does not change the physics of the problem.

B. High-order harmonic generation obtained from the calculation of an independent-electron Floquet-Hamiltonian eigenstate

To treat the time-periodicity symmetry of the Hamiltonian, we employ the Floquet theorem and method.^{31,32} It implies that for time periodic Hamiltonians, the solution of the time dependent Schrödinger equation can be written as $\exp(-i\epsilon^{QE}t/\hbar)\psi(t)$, where $\psi(t)$ is time periodic. ϵ^{QE} and ψ are the corresponding eigenvalue [quasienergy (QE)] and eigenfunction (Floquet state) of the single-electron Floquet Hamiltonian,

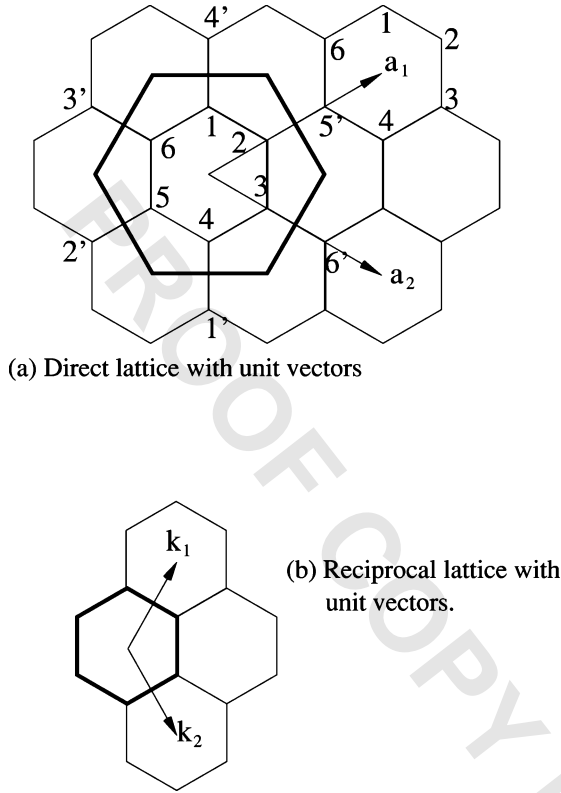


FIG. 1. (a) The symmetry-adapted unit cell of graphene is marked by the thick hexagon. This is not the most basic unit cell. However it is the smallest unit cell which possesses the C_6 symmetry when the TB approach is employed. $\vec{a}_1 = [(3\sqrt{3}/2)b, \frac{3}{2}b]$, and $\vec{a}_2 = [(3\sqrt{3}/2)b, -\frac{3}{2}b]$ are the corresponding unit vectors, where b is the bond length between two adjacent carbon atoms. \vec{a}_1 , and \vec{a}_2 are $\sqrt{3}$ times longer than the conventional ones and therefore the unit-cell area is three times larger than the conventional two-atom unit cell. (b) The first BZ is the area bounded by the thick hexagon. $\vec{b}_1 = p(2\pi/3\sqrt{3}b), 2\pi/3b]$, and $\vec{b}_2 = [(2\pi/3\sqrt{3}b), -2\pi/3b]$ are the corresponding unit vectors in the reciprocal lattice. \vec{b}_1, \vec{b}_2 are $\sqrt{3}$ -time shorter than the conventional ones and therefore the area of the first BZ is $1/3$ than that of the two-atom primitive unit cell.

$$\hat{H}_f(t)\psi(t) = \varepsilon^{QE}\psi(t), \quad (1)$$

which is given by

$$\hat{H}_f(t) = \frac{\hbar}{i} \frac{\partial}{\partial t} + \hat{H} - \frac{e}{c} \vec{A}(t) \cdot \vec{P}. \quad (2)$$

Here, $\hat{H} = (\hat{P}^2/2m) + \hat{V}(r)$ is the field-free Hamiltonian, e and m are the charge and mass of the electron, respectively, \vec{P} is the momentum operator, and $\hat{V}(r)$ reflects the spatial symmetry of the target. For convenience, the graphene monolayer is placed in the x - y plane. $\vec{A}(t)$ is the vector potential,

$$\vec{A}(t) = \sqrt{2}A_0[\cos(\theta)\cos(\omega t), \sin(\theta)\sin(\omega t), 0], \quad (3)$$

propagating in the z direction. For $\theta = 0, \pi/4$ and $\pi/2$ the field represented by $\vec{A}(t)$ is linearly polarized in the x direction,

and circularly polarized and linearly polarized in the y direction, respectively. For other values of θ , i.e., whenever $0 < \theta < \pi/2$, $\vec{A}(t)$ represents elliptically polarized light. The prefactor $\sqrt{2}$ is chosen such that circular polarization is given by $\vec{A}(t) = A_0[\cos(\omega t), \sin(\omega t), 0]$. Note that the dynamics of driven electrons in the x - y plane [i.e., neglecting the spatial z dependence of field (3)] is justified for thin targets and the medium-ranged laser intensities employed below, namely, $I_0 < 6 \times 10^{13}$ W/cm² (also see Refs. 19,20 and 29).

The HHGS ($I^{(n)}$) is obtained from the Fourier transform of the time-dependent acceleration

$$I^{(n)} \propto \left| \int_0^\infty e^{-in\omega t} \vec{d}(t) dt \right|^2, \quad (4)$$

where the time-dependent dipole moment $\vec{d}(t)$ is conventionally defined as

$$\vec{d}(t) = \langle \psi(r,t) | e\vec{r} | \psi(r,t) \rangle, \quad (5)$$

and $n\omega$ is the emitted harmonic frequency. In the following subsections we explain how the calculations are carried out for our specific (symmetry-adapted) problem.

C. Calculation of the quasienergy bands of graphene exposed to strong laser field

It is convenient to choose our basis functions as eigenfunctions of the symmetry operators commuting with the Floquet Hamiltonian (2). Since graphene possesses translation symmetries and the vector potential $\vec{A}(t)$ is homogeneous in the x - y plane, our starting point is the Bloch theorem

$$\hat{T}_{\vec{a}} \kappa(\vec{r}) = \kappa(\vec{r} + \vec{a}) = e^{i\vec{k} \cdot \vec{a}} \kappa(\vec{r}). \quad (6)$$

Here, $\hat{T}_{\vec{a}}$ is the translation operator, $\vec{a} = n_1 \vec{a}_1 + n_2 \vec{a}_2$ where \vec{a}_1 and \vec{a}_2 are the unit vectors of the symmetry-adapted lattice [see Fig. 1(a)], and \vec{k} is the wave vector in the first BZ of the reciprocal lattice [see Fig. 1(b)].

Within the TB approach,³⁰ $\kappa_{j\alpha}$ is written in terms of atomic orbitals of carbon, such that

$$\kappa_{j\alpha} = \frac{1}{\sqrt{N}} \sum_{n_1, n_2} e^{i\vec{k} \cdot \vec{R}_{\alpha, n_1, n_2}} \Psi_{j\alpha}(\vec{r} - \vec{R}_{\alpha, n_1, n_2}). \quad (7)$$

Here, $\Psi_{j\alpha}$ stand for the $2s$ ($j=1$), $2p_x$ ($j=2$), $2p_y$ ($j=3$) and $2p_z$ ($j=4$) type atomic orbitals and $\alpha=1, \dots, 6$ denotes the carbon atom in the symmetry-adapted unit cell [see Fig. 1(a)]. N is the total number of hexagonal unit-cells in the 2D cluster and it enters into Eq. (7) as the normalization prefactor of $\kappa_{j\alpha}$. The sum in Eq. (7), denoted by $\{n_1, n_2\}$, runs over all unit cells. The coordinates of atom α in the (n_1, n_2) th unit cell are related to the coordinates of the α atom in the reference unit cell by the simple relation

$$\vec{R}_{\alpha, n_1, n_2} = \vec{R}_{\alpha, 0, 0} + n_1 \cdot \vec{a}_1 + n_2 \cdot \vec{a}_2. \quad (8)$$

The eigenfunctions of \hat{T}_a^- , (i.e., $\{\kappa_{j\alpha}\}$) form the basis set that is used for the construction of the time-dependent Floquet wavefunctions.

The time-dependent Hamiltonian matrix representing the interaction of graphene with circularly-polarized laser field (the polarization plane is x - y) with the frequency ω and vector potential amplitude A_0 is given by

$$\mathcal{H}(\vec{k})(t) = \mathbf{H}(\vec{k}) + A_0 \mathbf{P}_x(\vec{k}) \cos(\omega t) + A_0 \mathbf{P}_y(\vec{k}) \sin(\omega t), \quad (9)$$

where \vec{k} is the wave vector in the reciprocal lattice. The matrices $\mathbf{H}(\vec{k})$, $\mathbf{P}_x(\vec{k})$, and $\mathbf{P}_y(\vec{k})$ are presented in Appendix A.

In our calculation we use the eigenfunctions of the field-free Hamiltonian matrix of graphene as basis functions, i.e.,

$$\mathbf{H}(\vec{k}) \mathbf{C}(\vec{k}) - \mathbf{S}(\vec{k}) \mathbf{C}(\vec{k}) \mathbf{E}(\vec{k}) = 0, \quad (10)$$

where $\mathbf{E}(\vec{k})$ is a diagonal eigenvalue matrix which provides the field-free EB structure of the model Hamiltonian for graphene, and $\mathbf{S}(\vec{k})$ is the overlap matrix of the basis functions $\kappa_{j\alpha}$ [see Eq. (7)]. Equation (10) is then transformed to the equivalent orthogonal eigenvalue problem

$$\tilde{\mathbf{H}}(\vec{k}) \tilde{\mathbf{C}}(\vec{k}) - \tilde{\mathbf{C}}(\vec{k}) \mathbf{E}(\vec{k}) = 0, \quad (11)$$

where the transformed eigenvector matrix $\tilde{\mathbf{C}}(\vec{k})$ is given by

$$\tilde{\mathbf{C}}(\vec{k}) = (\mathbf{S}(\vec{k}))^{1/2} \mathbf{C}(\vec{k}),$$

and the Hamiltonian matrix is given by

$$\tilde{\mathbf{H}}(\vec{k}) = (\mathbf{S}(\vec{k}))^{-1/2} \mathbf{H}(\vec{k}) (\mathbf{S}(\vec{k}))^{-1/2}.$$

The Floquet-Bloch QE states are obtained by solving the eigenvalue problem

$$\left(-i\hbar \frac{\partial}{\partial t} + \mathbf{E}(\vec{k}) + A_0 \mathcal{P}_x(\vec{k}) \cos(\omega t) + A_0 \mathcal{P}_y(\vec{k}) \sin(\omega t) \right) \mathbf{D}(\vec{k}) = \mathbf{D}(\vec{k}) \boldsymbol{\varepsilon}(\vec{k}), \quad (12)$$

where $\mathcal{P}_x(\vec{k})$ and $\mathcal{P}_y(\vec{k})$ are the transformed momentum matrices given by

$$\mathcal{P}_{(x,y)}(\vec{k}) = (\mathbf{C}(\vec{k}))^{-1} (\mathbf{S}(\vec{k}))^{-1} \cdot \mathbf{P}_{(x,y)}(\vec{k}) \cdot \mathbf{C}(\vec{k}).$$

The QEBs are uniquely determined only in the interval of, say, 0 to $\hbar\omega$. Therefore, they cannot be used to identify the filled states. Thus, we order them according to the expectation value of the time-dependent Hamiltonian with respect to the Floquet(-Bloch) states (see, e.g., Ref. 33),

$$\begin{aligned} \varepsilon_l(\vec{k}) &= \frac{1}{T} \int_0^T dt (\tilde{D}_l(\vec{k}))^\dagger \left(-i\hbar \frac{\partial}{\partial t} \right) \tilde{D}_l(\vec{k}) \\ &= \frac{1}{T} \int_0^T dt (\tilde{D}_l(\vec{k}))^\dagger [\mathbf{E}(\vec{k}) + A_0 \mathcal{P}_x(\vec{k}) \cos(\omega t) \\ &\quad + A_0 \mathcal{P}_y(\vec{k}) \sin(\omega t)] \tilde{D}_l(\vec{k}), \end{aligned} \quad (13)$$

a *single-value* mean-energy criterion utilized by Faisal and Kamiński²⁰ and Martinez *et al.*³⁴ to order QEBs. Equation (13) has been derived from the definition of the mean energy for the time dependent Hamiltonian, $\hat{H}(t)$, as $\langle\langle \psi(t) | \hat{H}(t) | \psi(t) \rangle\rangle = \langle\langle \psi(t) | -i\hbar (\partial/\partial t) | \psi(t) \rangle\rangle$ where $\langle\langle \dots \rangle\rangle$ stands for the integral over time (i.e., $1/T \int_0^T dt \dots$), where T is the period of the oscillating electronic field, and over space (i.e., $\int_0^\infty d\vec{r} \dots$).

Now it is possible to quantify the effect of the field on the electronic band structure of graphene by comparing the field-free EBs to the single-valued mean QEBs. On top of that, we can fill in the QEBs with electrons,^{13,20} analogously to occupying the EB's with electrons in the field-free case.

The QEBs (i.e., the field-distorted EBs) $\boldsymbol{\varepsilon}(\vec{k})$ are calculated by the (t, t') method as developed in Ref. 35. The (t, t') method enables one to express the time evolution operator $\hat{u}(t, 0)$ in an analytical form, $\hat{u}(t, 0) = \exp(-i\hat{H}_f(t')t)|_{t'=t}$. The numerical advantage of using the (t, t') method is that only a small number of Fourier basis functions $\exp(i\omega t')$ is needed to construct the Floquet matrix and still get accurate results, even for very strong laser fields. For field intensities when direct diagonalization requires the use of hundreds or even thousands of $\exp(i\omega t')$ basis functions, using the (t, t') method we need only up to 25 Fourier basis function. For details see Refs. 35 and 36.

D. Calculation of the high-order harmonic generation spectra

The probability to emit the n th harmonic is proportional to the Fourier component of the acceleration of the electron, see Eq. (4). Hence, within the independent-electron picture (equivalent to the Hartree approximation as employed in Refs. 8, 13, 19 and 20), the probability to get the n th harmonic is given by

$$\begin{aligned} I^{(n)} &\propto n^2 \left| 2 \times \sum_{\text{filled QEB's}} \langle\langle \langle \psi(\vec{k}, \vec{r}, t) | \hat{P}_x e^{-in\omega t} | \psi(\vec{k}, \vec{r}, t) \rangle \rangle \rangle \right|^2 \\ &\quad + n^2 \left| 2 \times \sum_{\text{filled QEB's}} \langle\langle \langle \psi(\vec{k}, \vec{r}, t) | \hat{P}_y e^{-in\omega t} | \psi(\vec{k}, \vec{r}, t) \rangle \rangle \rangle \right|^2 \\ &= n^2 \left| 2 \sum_{\text{filled QEB's}} \int d\vec{k} \int_0^T dt e^{-in\omega t} (\tilde{D}_l(\vec{k}))^\dagger \mathcal{P}_x(\vec{k}) \tilde{D}_l(\vec{k}) \right|^2 \\ &\quad + n^2 \left| 2 \times \sum_{\text{filled QEB's}} \int d\vec{k} \int_0^T dt e^{-in\omega t} \right. \\ &\quad \left. \times (\tilde{D}_l(\vec{k}))^\dagger \mathcal{P}_y(\vec{k}) \tilde{D}_l(\vec{k}) \right|^2, \end{aligned} \quad (14)$$

where \hat{P}_x and \hat{P}_y are the momentum operators in the x and y directions, respectively. The triple bra-ket notation stands for integration over time (t), space (\vec{r}) and crystal quasimomentum (\vec{k}) within the first BZ. The summation is over filled (single-valued) mean QEBs where multiplication by two accounts for the electron spin. The $\mathcal{P}_x(\vec{k})$, $\mathcal{P}_y(\vec{k})$ and $\mathbf{D}(\vec{k})$ matrices are as defined in Eq. (12). The rationale behind Eq.

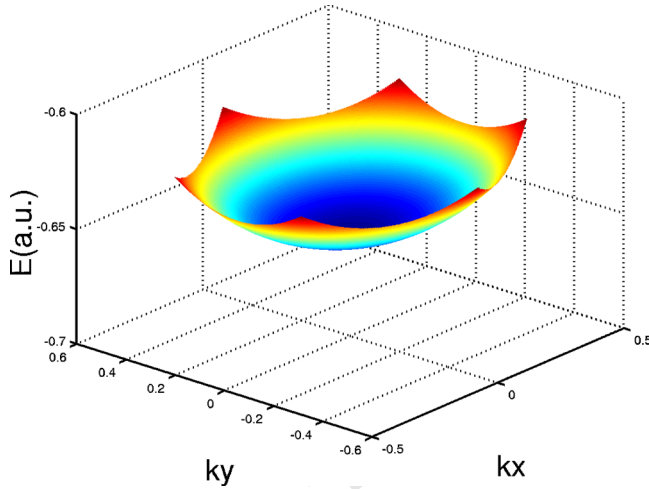


FIG. 2. (Color on-line) The lowest (σ -type) EB of graphene obtained by using the field-free TB Hamiltonian matrix and solving the eigenvalue problem (10). The C_{6v} symmetry, inherited from the real-space unit-cell symmetry, is clearly seen.

(14) that has been used also in Refs. 13 and 20 is based on classical arguments. Accelerated charged particles emit a high frequency radiation Ω with a probability amplitude which is proportional to the Fourier transform of the acceleration. In quantum mechanics, the square of the Fourier transform of the first derivative of the expectation value of the momentum operators provides the probability $I^{(n)}$ to emit coherent radiation with the frequency $\Omega = n\omega$.

For the integration over the quasimomentum \vec{k} we divide the hexagonal-shaped BZ into 12 equivalent parts, because the QEBs also possess a C_{6v} symmetry³⁷ (also see below). All quasimomentum vectors within the first BZ are picked up using random number generator within one of the parts. Equal number of vectors are generated within other parts by

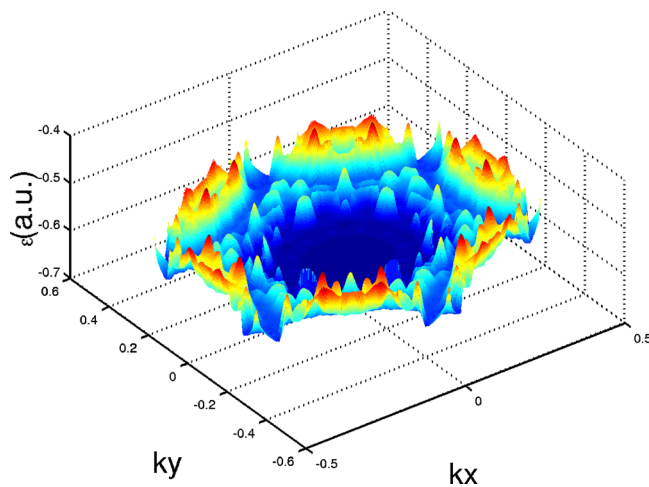


FIG. 3. (Color on-line): The lowest single-valued (mean) QEB of graphene [see Eq. (13)] exposed to circularly polarized field for the field intensity of $I_0 = 5.70 \times 10^{13}$ W/cm² and wavelength $\lambda = 800$ nm. The C_{6v} symmetry of the ground EB (see Fig. 4) is preserved. However, any other resemblance to the lowest EB is destroyed for such a strong intensity.

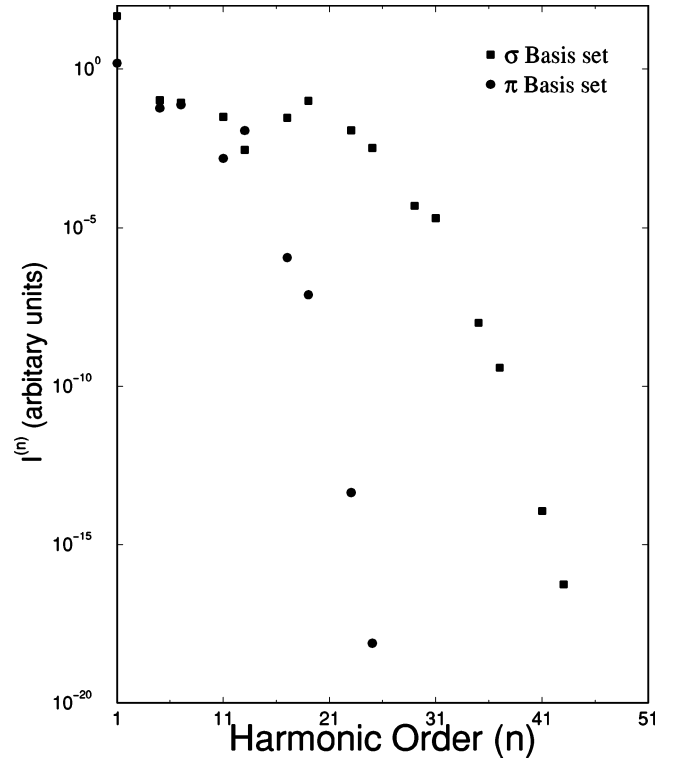


FIG. 4. The HGS for circularly polarized light using a σ -type basis set (which consists of carbon $2s$, $2p_x$ and $2p_y$ orbitals) and π -type basis set (which consists of carbon $2p_z$ orbitals). The length of the plateau in the case of the π -type basis set is about half that for the σ -type basis set. Hence, the HHG from graphene is dominated by the bound-bound transitions between σ -type orbitals. The laser frequency and intensity are, respectively, $\lambda = 800$ nm and $I_0 = 5.70 \times 10^{13}$ W/cm².

60° rotations and reflections. Hence, the correct symmetry is maintained throughout the calculations.

III. RESULTS AND DISCUSSION

To begin with, we would like to get a grasp at the effect of the laser field on the electronic structure of graphene. The ground EB of graphene, $E^{(0)}(\vec{k})$, is shown in Fig. 2. As known from the theory of space (plane) groups (see, e.g., Ref. 38), it possesses in reciprocal space the C_{6v} symmetry of the real-space unit cell. The lower single-valued mean QEB [see Eq. (13)] for graphene exposed to a high-intensity circularly polarized laser field ($\lambda = 800$ nm and $I_0 = 5.70 \times 10^{13}$ W/cm²) is depicted, for comparison, in Fig. 3. As is expected on the basis of the DS-based properties of the FB Hamiltonian,³⁷ the EB symmetry C_{6v} is preserved in the (mean) QEB. The “smooth landscape” of the field-free EB, on the other hand, is completely distorted at this field intensity, similar to the behavior obtained by Faisal and Kamiński for the 1D Kronig-Penney-type models.²⁰

We next proceed to the calculations of the HHGS for various intensities and polarizations. For comparison purposes, the calculations are done for two cases: In one case we use $2s$, $2p_x$, and $2p_y$ (σ -type) orbitals as the atomic orbital basis set and in another case $2p_z$ (π -type) orbitals are used.

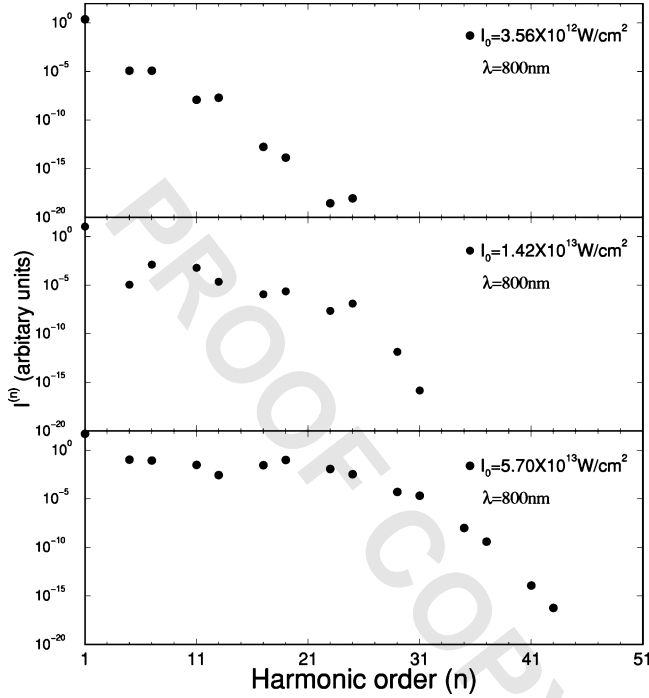


FIG. 5. The effect of variation of the intensity of the circularly polarized light on the HHGS for $\lambda = 800$ nm. (Top panel) For $I_0 = 3.56 \times 10^{12}$ W/cm² the $m=2$ harmonic pair is clearly found within the plateau, that is, the 11th and 13th harmonics can be measured. (Middle panel) Starting from $I_0 = 10^{13}$ W/cm², the $m=4$ harmonics, that is the 23rd and 25th harmonics, can be measured. (Bottom panel) Similarly, for $I_0 = 5.70 \times 10^{13}$ W/cm² the plateau extends to the 29th and 31st harmonics.

As stated above, these two basis sets do not couple within the chosen irradiation geometry. Figure 4 presents a comparison between the σ - and π -type basis sets for $\lambda = 800$ nm and $I_0 = 5.70 \times 10^{13}$ W/cm². The main difference is that the HHG cutoff is much shorter for the $2p_z$ electrons (π -basis set), i.e., the HOHs are generated by the electrons occupying the σ -type orbitals, what corroborates the inequality $|P_{x,\sigma}| < |P_{x,\pi}|$ that the dipole matrix elements satisfy (see Table III in Appendix B). When circularly polarized light is applied, the HHGS is obtained due to transitions between bound states (so-called bound-bound transitions).^{9,12} In the TB model these bound-bound transitions are governed by the magnitude of the electron dipole matrix elements. Since the π -type dipole matrix parameters are smaller than the σ -type ones, it is expected that the electrons in the π -type orbitals do not involve in the generation of HOHs as much as the σ electrons do. This explains the results presented in Fig. 4. Hereafter, when it is not specifically mentioned, the results presented are for the σ -type orbitals only.

Next, the effect of the laser intensity (and frequency) is studied for $\lambda = 800$ and 1250 nm. In the case of the “three-step model” associated with atomic targets, where the HOHs are generated by a linearly-polarized light due to the bound-continuum transitions,³⁹ the HHG cutoff n_{cutoff} increases linearly with respect to the intensity of the field, i.e., $\hbar \omega n_{cutoff} \propto I_0 / \omega^2$.³⁹ However, in our studied case where circularly polarized light is applied, the HOHs are generated by

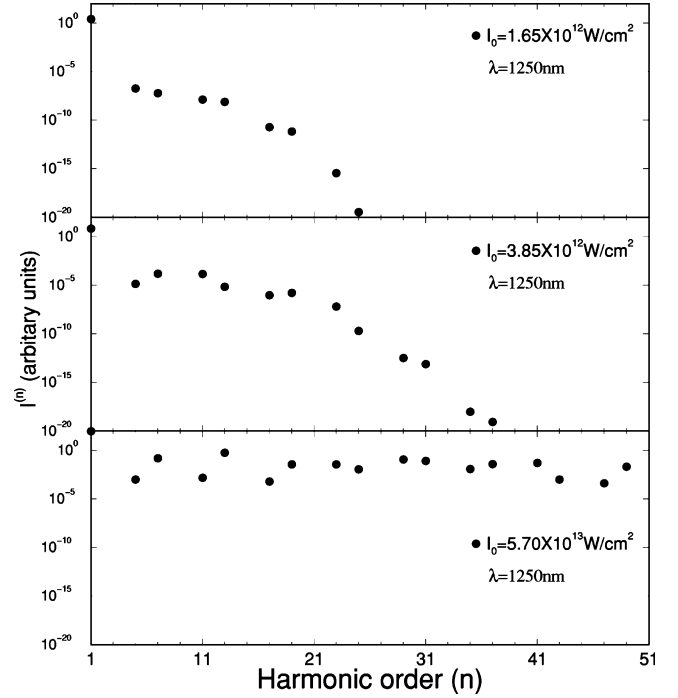


FIG. 6. The effect of variation of the intensity of the circularly polarized light on the HHGS for $\lambda = 1250$ nm. (Top panel) For $I_0 = 1.65 \times 10^{12}$ W/cm² the $m=2$ harmonic pair is clearly found within the plateau, that is the 11th and 13th harmonics can be measured. (Middle panel) Starting from $I_0 = 3.85 \times 10^{12}$ W/cm², the $m=3$ harmonics, that is the 17th and 19th harmonics, can be measured. (Bottom panel) However, at the intensity of 5.70×10^{13} W/cm² the plateau extends to the 59th and 61st harmonics (not shown in the plot).

another mechanism, namely due to bound-bound transitions.⁹ In this case (see Refs. 9 and 12), n_{cutoff} increases linearly with respect to the field amplitude $E_0 = \omega A_0$, i.e., $n_{cutoff} \propto E_0 / \omega \propto \sqrt{I_0} / \omega$, rather than with respect to the pondermotive potential as mentioned above for the atomic case.³⁹ Interestingly, Pronin *et al.*²⁷ found a similar cutoff dependence (reflecting a bound-bound transition mechanism) for HHG by a 1D model of a superlattice in a linearly polarized field. Indeed, our numerical results for graphene (a crystalline monolayer) confirm these expectations. In Figs. 5 and 6 we present, respectively, the HHGS for three different intensities when $\lambda = 800$ and 1250 nm. The minimum intensities which produce a plateau (with the $m=2$ harmonic pair) in the HHGS are, respectively, $I_0 = 3.56 \times 10^{12}$ and 1.65×10^{12} W/cm² for $\lambda = 800$ and 1250 nm. A simple extension of the plateau, following the above-mentioned scaling law, is obtained for $I_0 = 1.42 \times 10^{13}$ W/cm² and $\lambda = 800$ nm at $n_{cutoff} = 23-25$ ($m=4$) and, for a nearly four-times lower intensity of $I_0 = 3.85 \times 10^{12}$ W/cm² and $\lambda = 1250$ nm at $n_{cutoff} = 17-19$ ($m=3$). For higher intensity of $I_0 = 5.70 \times 10^{13}$ W/cm², the HHG cutoff is at $n_{cutoff} = 29-31$ ($m=5$) when $\lambda = 800$ nm whereas it is at $n_{cutoff} = 59-61$ ($m=10$; not shown in the plot) when $\lambda = 1250$ nm. Therefore, to observe a longer plateau it is preferable to carry out the experiments using a high intensity laser with a wavelength of 1250 nm rather than with an 800-nm one. This result cor-

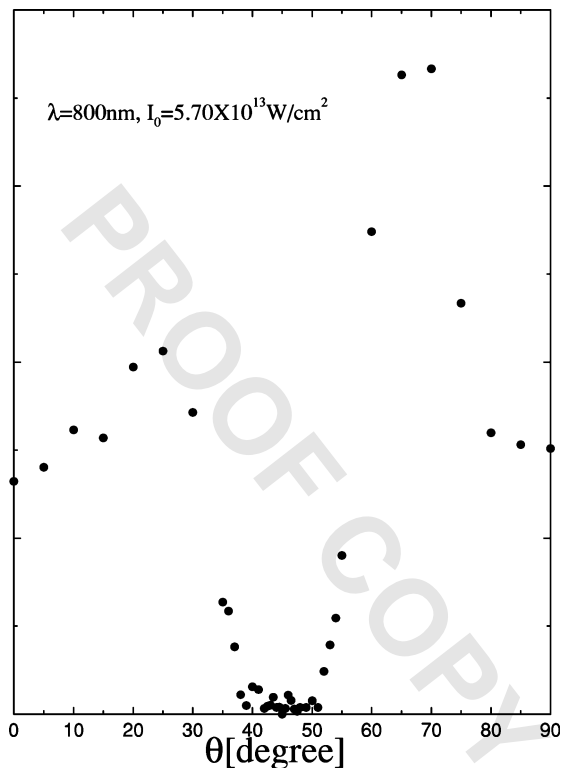


FIG. 7. The ratio of the third and fifth harmonics vs the ellipticity parameter θ [see Eq. (3)] for $I_0=5.70\times 10^{13}$ W/cm² and wavelength $\lambda=800$ nm. For linearly polarized light, $\theta=0$, this ratio is about 0.15. For $40^\circ < \theta < 50^\circ$, the ratio is less than 0.015 and for $44^\circ < \theta < 46^\circ$, the ratio is almost equal to zero. Hence, the SRs in circularly polarized fields are quite robust to imperfect circular polarization.

roborates the analytical proof based on the assumption that the photo-induced ionization is small and assuming Hückel molecular orbital energies,⁹ as well as the results of recent calculations of HHG from oriented benzene.¹² The physical explanation for this effect, as detailed in Ref. 9 for circularly polarized fields (also see Ref. 40 for a similar bound-bound dynamics of dissociating molecular ions in a linearly-polarized field), goes as follows. When bound-bound transitions govern the HHG process, the interaction energy with the field (charge \times dipole strength \times field amplitude) is transformed to HOHs. The interaction energy *does not* depend on the fundamental frequency. Therefore, the length of the plateau n_{cutoff} (which is equal to the maximal variation of the interaction energy, divided by the fundamental photon energy) increases with λ .⁹ Following the discussion at the Introduction and Refs. 23 and 24, one should expect that the HHG from thin graphite films can be induced with sub-20-fs IR laser pulses with intensities not exceeding $I_0 = 10^{13}$ W/cm² before qualitative damage and structural changes occur. Since for intensities above 10^{13} W/cm² the graphite film could be destroyed, to obtain a continuous generation of HOHs at these intensities the laser focus should translate along the sample.

The stability of the SRs to imperfect circular polarization is studied next. In Fig. 7 the ratio of the third and fifth harmonic intensities for $\lambda=800$ nm and $I_0=5.70$

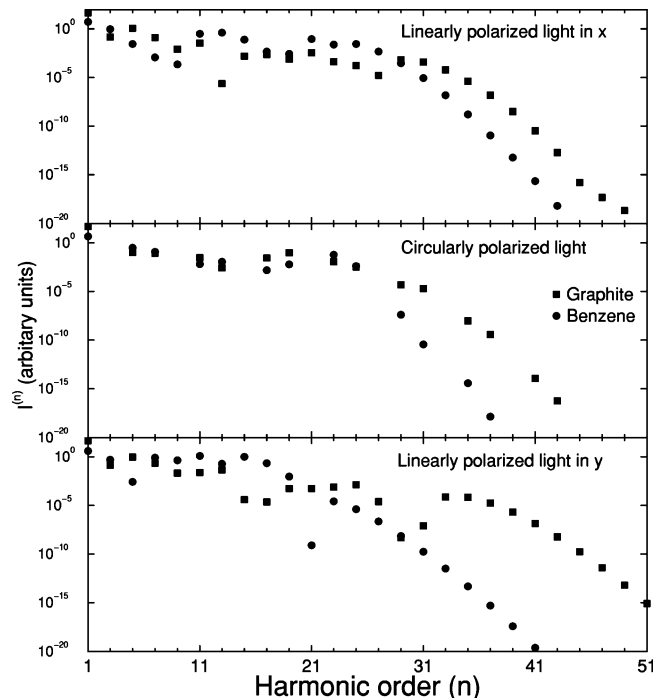


FIG. 8. (Top panel) The HHGS of graphene and benzenelike molecule (one unit cell of graphene) for light linearly polarized in the x direction ($\theta=0$). (Middle panel) Circularly polarized in the x directions light ($\theta=\pi/4$). (Bottom panel) Light linearly polarized in the y direction ($\theta=\pi/2$). The cutoffs in the three HHGS are about the same for both systems for the different polarizations of the light. Within the framework of the FTB method, the length of the plateau for “benzene” is shorter than that of graphene.

$\times 10^{13}$ W/cm² is displayed as a function of the ellipticity parameter θ [see Eq. (3)]. For linearly polarized light, $\theta=0$, this ratio is about 0.15. This is an interesting result which indicates the strong non-linearity of the photoinduced dynamics when the strong laser field is applied, regardless of the polarization of the laser. A microscopic explanation of this result requires further investigations which are beyond the scope of the present work. Notwithstanding, such a phenomena have been observed in recent experiments.⁴¹ Interestingly, *already* for $40^\circ < \theta < 50^\circ$ this ratio is less than 0.015 and for $44^\circ < \theta < 46^\circ$ it is almost equal to zero. Since the degree of circular polarization can be easily controlled to within $\Delta\theta < 1^\circ$, the conclusion is clear; The SRs are very stable when changing the ellipticity in the vicinity of the perfect circular polarization ($\theta=45^\circ$) and, thus, are expected to be observed in experiments.

To estimate the effect of employing extended periodic systems (i.e., thin graphite films) on the HHGS we performed, for comparison, the calculation for a benzenelike molecule (benzene without hydrogen atoms). Figure 8 shows the HHGSs for graphene and for a benzene like system interacting with circularly polarized light and with light linearly polarized in the x and y directions. The difference in HHGSs obtained for light linearly polarized in x and y directions results from the different orientations with respect to the polarization vectors of the unit cell in the x - y plane. In order to maximize the polarization effect on the HHGS (for

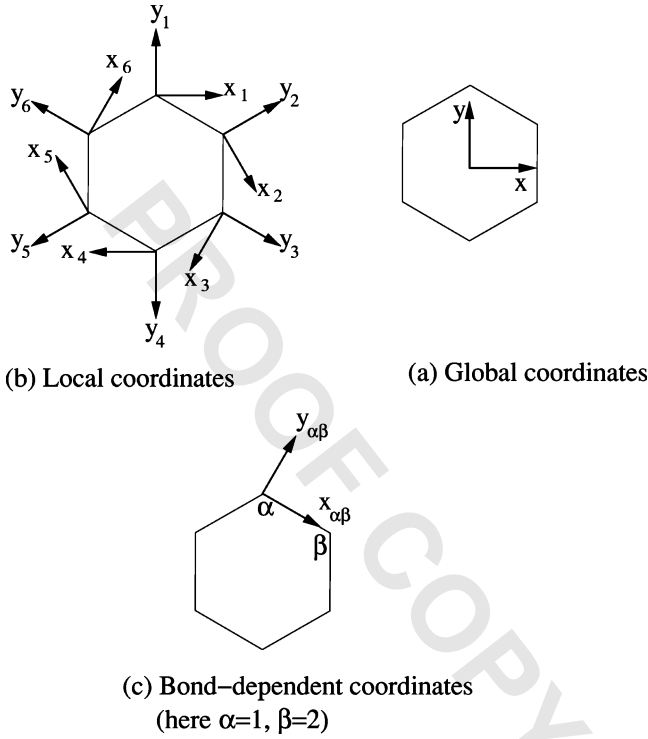


FIG. 9. Three types of coordinate systems discussed in Appendix A are illustrated: (a) Global coordinates (x, y) . (b) Atom-position-dependent local coordinates (x_α, y_α) , where y_α is directed towards the center of the unit cell and x_α is perpendicular to it. (c) Bond-dependent coordinates $(x_{\alpha-\beta}, y_{\alpha-\beta})$, where $y_{\alpha-\beta}$ is perpendicular to the bond connecting atoms α with β , and $x_{\alpha-\beta}$ is along the bond.

illustrative purpose) we represent the results for $I_0=5.70 \times 10^{13} \text{ W/cm}^2$. We observe that the harmonic generation of the benzene like structure dies off relatively faster than that of graphene for circularly-polarized light as well as for light linearly polarized in the x and y directions. Therefore, employing an extended periodic structure for the generation of HOHs would result in extended plateaus in comparison to a molecular system.

IV. SUMMARY

A FTB approach has been developed for the calculation and study of HHGSs from spatially periodic targets. Our calculations show that the HHGSs obtained for graphene interacting with *nonperturbative* circularly polarized IR light ($\lambda=800$ and 1250 nm) admit several attractive properties. In particular, the DS-based SRs for C_n symmetry and circularly polarized fields are found to be valid for this laser-target system. For graphene ($n=6$) the calculation clearly shows the emitted frequencies are Ω (emitted) $= (6n \pm 1)\omega$, $n=1, 2, 3, \dots$. The HHGS is rather stable to the variation of the elliptical angle of the polarization $\theta=45^\circ \pm 5^\circ$. Note that in a typical experiment the ellipticity θ can be easily controlled with an accuracy of $\Delta\theta < 1^\circ$. The DS-based SRs for the HHGS are found to be pronounced, i.e., a clear extended

$\langle s(\beta) \hat{H} s(\alpha) \rangle = H_{ss}$	$\langle s(\alpha) \hat{H} p_{x,\alpha}(\beta) \rangle = H_{sp}$	$\langle s(\alpha) \hat{H} p_{y,\alpha}(\beta) \rangle = 0$
$\langle s(\beta) \hat{P}_{x,\alpha} s(\alpha) \rangle = P_{x,ss}$	$\langle s(\alpha) \hat{P}_{x,\alpha} p_{x,\alpha}(\beta) \rangle = P_{x,sp}$	$\langle s(\alpha) \hat{P}_{x,\alpha} p_{y,\alpha}(\beta) \rangle = 0$
$\langle s(\beta) \hat{P}_{y,\alpha} s(\alpha) \rangle = 0$	$\langle s(\alpha) \hat{P}_{y,\alpha} p_{x,\alpha}(\beta) \rangle = 0$	$\langle s(\alpha) \hat{P}_{y,\alpha} p_{y,\alpha}(\beta) \rangle = P_{y,sp}$
$\langle p_{x,\alpha}(\beta) \hat{H} p_{x,\alpha}(\alpha) \rangle = -H_v$	$\langle p_{y,\alpha}(\beta) \hat{H} p_{y,\alpha}(\alpha) \rangle = H_\pi$	$\langle p_{x,\alpha}(\beta) \hat{H} p_{y,\alpha}(\alpha) \rangle = 0$
$\langle p_{x,\alpha}(\beta) \hat{P}_{x,\alpha} p_{x,\alpha}(\alpha) \rangle = P_{x,\sigma}$	$\langle p_{y,\alpha}(\beta) \hat{P}_{x,\alpha} p_{y,\alpha}(\alpha) \rangle = P_{x,\pi}$	$\langle p_{x,\alpha}(\beta) \hat{P}_{x,\alpha} p_{y,\alpha}(\alpha) \rangle = 0$
$\langle p_{x,\alpha}(\beta) \hat{P}_{y,\alpha} p_{x,\alpha}(\alpha) \rangle = 0$	$\langle p_{y,\alpha}(\beta) \hat{P}_{y,\alpha} p_{y,\alpha}(\alpha) \rangle = 0$	$\langle p_{x,\alpha}(\beta) \hat{P}_{y,\alpha} p_{y,\alpha}(\alpha) \rangle = P_{y,\pi}$

FIG. 10. The matrix elements for atomic orbitals, when the orbitals are described in bond-dependent coordinates. In our problem, we choose to describe the atomic orbitals in local-dependent coordinates. Hence, we need to project the atomic orbitals expressed in local-dependent coordinates into orbitals expressed in bond-dependent coordinates.

plateau in HHGS is predicted for the studied field intensities of $1.65 \times 10^{12} \leq I_0 \leq 5.70 \times 10^{13} \text{ W/cm}^2$ for a $\lambda = 1250$ nm laser, and $1.42 \times 10^{13} \leq I_0 \leq 5.70 \times 10^{13} \text{ W/cm}^2$ for a $\lambda = 800$ nm laser.

The generation of HOHs results mainly from the electrons occupying the σ -type orbitals. The fact that the contribution to the generation of HOHs from the electrons occupying the π -type orbitals is much smaller implies that one can expect that the DS-based SRs for the HHGSs (i.e., the ability to control the ratio between two successive—symmetry allowed and forbidden—odd harmonics) should not be strongly affected by the onset of ionization from the π -type orbitals.

It has been found that the HHGS has about the same cutoff regardless of the polarization direction. In other words, the use of circularly polarized light rather than a linearly polarized one acts like a filter and not as an amplifier. However, using graphene rather than a benzene like molecule, besides avoiding the need for and the complications associated with aligning molecules, also provides larger cut-offs in the HHGS, namely graphene (graphite) with respect to “benzene” acts like an amplifier. Consequently, it makes the control and generation of HOHs from thin graphite films to be experimentally attractive and feasible.

ACKNOWLEDGMENTS

This work was supported in part by the Basic Research Foundation administered by the Israeli Academy of Sciences and Humanities and by the Fund for the Promotion of Research at Technion. A.K.G. is grateful to the Aly Kaufmann fellowship and O.E.A. to the European Community (Marie-Curie fellowship) for financial supports. We wish to thank Dr. V. Averbukh and Professor J. Schirmer for most helpful discussions.

APPENDIX A: CONSTRUCTION OF THE FLOQUET HAMILTONIAN MATRIX ELEMENTS FOR LASER-DRIVEN GRAPHENE WITHIN THE FLOQUET-TIGHT-BINDING APPROACH

To calculate the matrix elements $\langle \kappa_{j\alpha} | \hat{O} | \kappa_{j'\beta} \rangle$, where \hat{O} represents the momentum \hat{P}_x , \hat{P}_y , the unit \hat{I} and the field-free Hamiltonian \hat{H} operators, we use three types of coordinate systems as depicted in Fig. 9: (a) Global coordinates (x, y) . (b) Atom-position-dependent local coordinates (x_α, y_α) , where y_α is directed toward the center of the unit cell and x_α is perpendicular to it. (c) Bond-dependent coordinates $(x_{\alpha-\beta}, y_{\alpha-\beta})$, where $y_{\alpha-\beta}$ is perpendicular to the bond connecting atoms α with β and $x_{\alpha-\beta}$ is along the bond. The z coordinate is always in the global frame [coordinate system (a)] for the 2D graphene lattice.

To simplify the calculation of the matrix elements, we choose to describe the atomic orbitals in the $\{x_\alpha, y_\alpha\}$ coordinates (i.e., local coordinates), namely,

$$\begin{aligned} |2s_\alpha\rangle &= \Psi_{1\alpha}(\vec{r} - \vec{R}_{\alpha, n_1, n_2}) \\ &= \left(\frac{1}{4\pi}\right)^{1/2} 2 \left(\frac{z_{2s}}{2a_0}\right)^{3/2} \left(1 - \frac{z_{2s}}{2} r\right) \exp\left(-\frac{z_{2s}}{2} r\right), \end{aligned} \quad (\text{A1})$$

$$\begin{aligned} |2p_{x\alpha}\rangle &= \Psi_{2\alpha}(\vec{r} - \vec{R}_{\alpha, n_1, n_2}) \\ &= \left(\frac{1}{4\pi}\right)^{1/2} \left(\frac{z_{2p}}{2a_0}\right)^{3/2} \left(\frac{z_{2p}}{a_0}\right) x \exp\left(-\frac{z_{2p}}{2} r\right), \end{aligned} \quad (\text{A2})$$

and similar expressions for $|2p_{y\alpha}\rangle$ and $|2p_{z\alpha}\rangle$ where y and z replace the x coordinate in Eq. (A2). Here, $r = |\vec{r} - \vec{R}_{\alpha, n_1, n_2}|$ and (x, y, z) are the Cartesian component of $(\vec{r} - \vec{R}_{\alpha, n_1, n_2})$. The effective nuclear charges, $z_{2s} = \sqrt{5.72}$ for $2s$ -type carbon orbitals and $z_{2p} = \sqrt{3.16}$ for $2p$ -type orbitals, take into account the screening effect of the electrons.⁴² We employ the TB approach where only nearest-neighbor interactions are considered, i.e.,

$$\begin{aligned} \langle \Psi_{j\alpha}(\vec{r} - \vec{R}_{\alpha, n_1, n_2}) | \hat{H} | \Psi_{j'\beta}(\vec{r} - \vec{R}_{\beta, n'_1, n'_2}) \rangle \\ = 0 \quad \text{if } j, j' \text{ are not neighbors,} \end{aligned} \quad (\text{A3})$$

where neighbors are carbon atoms which are connected by a chemical bond. The fact that $\langle \Psi_{j\alpha}(\vec{r} - \vec{R}_{\alpha, n_1, n_2}) | \hat{P} | \Psi_{j'\alpha+2}(\vec{r} - \vec{R}_{\alpha+2, n_1, n_2}) \rangle$ is smaller in some cases even by one order of magnitude than $\langle \Psi_{j\alpha}(\vec{r} - \vec{R}_{\alpha, n_1, n_2}) | \hat{P} | \Psi_{j'\alpha+1}(\vec{r} - \vec{R}_{\alpha+1, n_1, n_2}) \rangle$ justifies our use of the TB model Hamiltonian, where only nearest neighbor interactions are considered. In Fig. 10 we schematically show the matrix elements of the field-free Hamiltonian and momentum operators for the σ -type orbitals ($2s, 2p_x, 2p_y$).

In the local coordinate (x_α, y_α) representation (b), the matrix elements are invariant under the cyclic permutation of α and $\beta = \alpha + 1$. As an illustrative example, the matrix elements between two atomic orbitals centered at $\alpha = 2$ and $\beta = 3$ carbons are given in the end of this appendix. It is clear that all other matrix elements of non-neighboring atoms within the same unit cell ($n_1 = n'_1$ and $n_2 = n'_2$) vanish identically. For instance, $\langle \Psi_{j1} | \hat{H} | \Psi_{j3} \rangle = 0$. However, there are nonvanishing matrix elements due to the chemical bonding between two carbon atoms that belong to adjacent unit cells. The calculation of such matrix elements is straightforward.

Having evaluated the atomic-orbital-based matrix elements (see Fig. 10), we proceed to calculate the matrix elements for our basis functions:

$$\begin{aligned} O_{j\alpha, j'\beta}^{(k)} &= \langle \kappa_{j\alpha} | \hat{O} | \kappa_{j'\beta} \rangle \\ &= \frac{1}{N} \left\langle \sum_{n_1, n_2} e^{i\vec{k} \cdot \vec{R}_{\alpha, n_1, n_2}} \Psi_{j\alpha}(\vec{r} - \vec{R}_{\alpha, n_1, n_2}) | \hat{O} \right. \\ &\quad \left. \times \sum_{n'_1, n'_2} e^{i\vec{k} \cdot \vec{R}_{\beta, n'_1, n'_2}} \Psi_{j'\beta}(\vec{r} - \vec{R}_{\beta, n'_1, n'_2}) \right\rangle, \end{aligned} \quad (\text{A4})$$

where \hat{O} stands for the Hamiltonian \hat{H} or \hat{P}_x , \hat{P}_y and \hat{I} . From Fig. 1 one can see that the non-vanishing matrix elements can be divided into three different categories detailed below. Note that in order to simplify our calculation, we use local coordinates rather than global ones. Hence the momentum matrix element in the local coordinates has to be converted to momentum matrix element in global one using the simple rotation transformation

$$\begin{pmatrix} \hat{P}_x \\ \hat{P}_y \end{pmatrix} = \begin{pmatrix} \cos(\varphi) & \sin(\varphi) \\ -\sin(\varphi) & \cos(\varphi) \end{pmatrix} \begin{pmatrix} \hat{P}_{x_{\alpha-\beta}} \\ \hat{P}_{y_{\alpha-\beta}} \end{pmatrix}, \quad (\text{A5})$$

where φ is the angle between the bond connecting the α and β carbons (i.e., bond-dependent coordinates) and the global-coordinate x axis. For the same reason, the Hamiltonian matrix elements associated with categories (ii) and (iii) below are different.

(i) The interacting orbitals are associated with the same carbon atom, i.e., $\alpha = \beta$. In this case $n_1 = n'_1$ and $n_2 = n'_2$ [see Eq. (A4)] since carbon α in one unit cell cannot have a chemical bond with the corresponding carbon α in another unit cell. Thus, the Hamiltonian matrix elements are given by

$$\begin{aligned} H_{j\alpha,j'\alpha}^{(k)} &= \frac{1}{N} \sum_{n_1, n_2} \langle \Psi_{j\alpha}(\vec{r} - \vec{R}_{\alpha, n_1, n_2}) | \hat{H} | \Psi_{j'\alpha}(\vec{r} - \vec{R}_{\alpha, n_1, n_2}) \rangle \\ &= \frac{1}{N} \sum_{n_1, n_2} \langle \Psi_{j\alpha}(\vec{r} - \vec{R}_{\alpha, 0, 0}) | \hat{H} | \Psi_{j'\alpha}(\vec{r} - \vec{R}_{\alpha, 0, 0}) \rangle \\ &= \langle \Psi_j | \hat{H} | \Psi_{j'} \rangle = \epsilon_j \delta_{jj'}, \end{aligned} \quad (\text{A6})$$

where $\epsilon_1 = \epsilon_{2s}$ and $\epsilon_2 = \epsilon_3 = \epsilon_4 = \epsilon_{2p}$. The orbital energies in atomic units (a.u.) are $\epsilon_{2s} = -0.326$ and $\epsilon_{2p} = 0$.³⁰ The corresponding nonzero matrix elements for momentum matrix elements [i.e., \hat{H} is replaced by $P_{x\alpha}$ or $P_{y\alpha}$ in Eq. (A6)] are (see also Fig. 10).

$$(p_{x\alpha})_{1,2} = (p_{y\alpha})_{1,3} = p,$$

where local atom (α) coordinates are used. We still can use Eq. (A5) for converting the matrix elements to global coordinates with $\varphi = (\alpha - 1)\pi/3$. The transition moment in a.u. is $p = \langle 2s | \hat{P}_x | 2p_x \rangle = \langle 2s | \hat{P}_y | 2p_y \rangle = 0.145i$. The others are equal to zero due to the symmetry properties of the atomic orbitals.

(ii) The interacting carbon atoms are α and β such that $\beta = \alpha + 1 - 6n$, where n is an integer number such that $1 \leq \beta \leq 6$. Following the same arguments as in case (i), the only nonzero elements are obtained when $n_1 = n'_1$ and $n_2 = n'_2$ (i.e., the two carbons are in the same unit cell). Therefore,

$$\begin{aligned} H_{j\alpha,j'\beta}^{(k)} &= \frac{1}{N} \sum_{n_1, n_2} e^{i\vec{k} \cdot (\vec{R}_{\beta, n_1, n_2} - \vec{R}_{\alpha, n_1, n_2})} \\ &\quad \times \langle \Psi_{j\alpha}(\vec{r} - \vec{R}_{\alpha, n_1, n_2}) | \hat{H} | \Psi_{j'\beta}(\vec{r} - \vec{R}_{\beta, n_1, n_2}) \rangle \\ &= \frac{1}{N} \sum_{n_1, n_2} e^{i\vec{k} \cdot (\vec{R}_{\beta, 0, 0} - \vec{R}_{\alpha, 0, 0})} \\ &\quad \times \langle \Psi_{j\alpha}(\vec{r} - \vec{R}_{\alpha, 0, 0}) | \hat{H} | \Psi_{j'\beta}(\vec{r} - \vec{R}_{\beta, 0, 0}) \rangle \\ &= e^{i\vec{k} \cdot (\vec{R}_{\beta, 0, 0} - \vec{R}_{\alpha, 0, 0})} \langle \Psi_j | \hat{H} | \Psi_{j'} \rangle \\ &= e^{i\vec{k} \cdot (\vec{R}_{\beta, 0, 0} - \vec{R}_{\alpha, 0, 0})} h_{jj'}, \end{aligned} \quad (\text{A7})$$

where $h_{jj'}$ are given in Table I of Appendix B.

Corresponding momentum matrix elements $(p_{(x,y)\alpha-\beta})_{jj'}$ are given in Table IV of Appendix B (also see Fig. 10). The

angle φ required to convert the matrix elements to the global coordinates is given by $\varphi = \pi/6 + (\alpha - 1)\pi/3$.

(iii) The two interacting carbons satisfy the condition $\beta = \alpha + 3 - 6n$, i.e., they are in different (neighboring) unit cells. For clarity, in Fig. 1 we denote by superscripts the carbons in adjacent cells that have a bond with carbons in the reference unit cell ($n_1 = n_2 = 0$). In this case we find

$$\begin{aligned} H_{j\alpha,j'\beta}^{(k)} &= e^{i\vec{k} \cdot (\vec{R}_{\alpha'} - \vec{R}_{\alpha})} \langle \Psi_{j\alpha}(\vec{r} - \vec{R}_{\alpha}) | \hat{H} | \Psi_{j'\alpha'}(\vec{r} - \vec{R}_{\alpha'}) \rangle \\ &= e^{i\vec{k} \cdot (\vec{R}_{\alpha'} - \vec{R}_{\alpha})} h_{jj'}. \end{aligned} \quad (\text{A8})$$

\vec{R}_{α} is the position vector of the carbon α in the reference unit cell whereas $\vec{R}_{\alpha'}$ is the position vector of the carbon β in the neighboring cell that has a chemical bond with carbon α in the reference cell [see Eq. (8)]. $h_{jj'}$ are given in Table II of Appendix B. Corresponding momentum matrix elements $(p_{(x,y)\alpha-\beta})_{jj'}$ are given in Table V of Appendix B. The angle φ needed to convert the matrix elements from bond-dependent to global coordinates is given by $\varphi = \pi/2 + (\alpha - 1)\pi/3$.

The values of the Hamiltonian- and overlap-integrals given in Table III of Appendix B, are taken from Ref. 30. The momentum matrix elements $P_{x\alpha-\beta}$ and $P_{y\alpha-\beta}$ are calculated by carrying out analytical differentiation of the orbitals [see Eqs. (A1) and (A2)] and the integrations over coordinate space are carried out numerically.

For the irradiation geometry chosen (this is also reflected by the data in Tables I, II, IV, and V of Appendix B), there are two independent blocks— σ and π —as is the case for the time-independent Hamiltonian.³⁰ The σ block couples the $2s$, $2p_x$, and $2p_y$ orbitals whereas the π block comprises of the $2p_z$ orbitals only. Since these two blocks do not mix, we separate accordingly the calculation for the HHGS. Consequently, the computational effort is, of course, reduced.

As an illustrative example, let us calculate the matrix elements between two atomic orbitals centered at $\alpha = 2$ and $\beta = 3$ carbons (see Fig. 1). First, we resolve the orbitals in terms of bond-dependent coordinates x_{2-3}, y_{2-3} (see Fig. 9); Then, using Fig. 10, we can calculate the matrix elements for the atomic orbitals; i.e., the Hamiltonian matrix element $\langle \Psi_{32} | \hat{H} | \Psi_{13} \rangle$ is given by

$$\begin{aligned} \langle \Psi_{32} | \hat{H} | \Psi_{13} \rangle &\equiv \langle 2p_{y_2} | \hat{H} | 2s_3 \rangle \\ &= \langle -p_{x_{2-3}} \cos(\pi/3) + p_{y_{2-3}} \sin(\pi/3) | \hat{H} | s_3 \rangle \\ &= -H_{sp} \cos(\pi/3). \end{aligned} \quad (\text{A9})$$

In a very similar way, the other matrix elements presented in Tables I, II, IV, and V of Appendix B are evaluated.

**APPENDIX B: MATRIX ELEMENTS FOR THE
FLOQUET HAMILTONIAN**

TABLE I. The matrix elements $h_{jj'}$ (as enter into Eq. (A7)) required for the calculations of the Hamiltonian matrix elements when the two interacting carbon atoms are neighbors and are in the same unit cell. The values of the matrix elements (H_{ss}, \dots, H_{π}) are given in Table III.

$h_{jj'}$	$j'=1$	$j'=2$	$j'=3$	$j'=4$
$j=1$	H_{ss}	$-H_{sp}\cos(\frac{\pi}{6})$	$-H_{sp}\cos(\frac{\pi}{3})$	0
$j=2$	$H_{sp}\cos(\frac{\pi}{6})$	$-H_{\sigma}\cos^2(\frac{\pi}{6})-H_{\pi}\sin^2(\frac{\pi}{6})$	$-H_{\sigma}\cos(\frac{\pi}{6})\cos(\frac{\pi}{3})+H_{\pi}\sin(\frac{\pi}{6})\sin(\frac{\pi}{3})$	0
$j=3$	$-H_{sp}\cos(\frac{\pi}{3})$	$H_{\sigma}\cos(\frac{\pi}{6})\cos(\frac{\pi}{3})-H_{\pi}\sin(\frac{\pi}{6})\sin(\frac{\pi}{3})$	$H_{\sigma}\cos^2(\frac{\pi}{3})+H_{\pi}\sin^2(\frac{\pi}{3})$	0
$j=4$	0	0	0	H_z

TABLE II. The matrix elements $h_{jj'}$ [as enter into Eq. (A8)] required for the calculations of the Hamiltonian matrix elements when the two interacting carbon atoms are neighbors but in different unit cells. The values of the matrix elements (H_{ss}, \dots, H_{π}) are given in Table III.

$h_{jj'}$	$j'=1$	$j'=2$	$j'=3$	$j'=4$
$j=1$	H_{ss}	0	H_{sp}	0
$j=2$	0	$-H_{\pi}$	0	0
$j=3$	H_{sp}	0	H_{σ}	0
$j=4$	0	0	0	H_z

TABLE III. Values of the matrix elements for graphene in atomic unit as defined in Fig. 10. The matrix elements associated with \hat{H} and \hat{S} are taken from Ref. 30. The other matrix elements are calculated numerically as described in the text at the end of Appendix A.

\hat{O}	\hat{H}	\hat{S}	\hat{P}_x/i	\hat{P}_y/i
O_{ss}	-0.24886	0.212	-0.133	0
O_{sp}	-0.2051	0.102	-0.0866	-0.178
O_{σ}	-0.18518	0.146	-0.368	0
O_{π}	-0.1115	0.129	-0.206	-0.206
O_z	-0.1115	0.129	-0.206	0

TABLE IV. The matrix elements of the $\hat{P}_{x_{\alpha-\beta}}$ and $\hat{P}_{y_{\alpha-\beta}}$ momentum operators in the bond-dependent coordinates [as enter into Eq. (A7), when the Hamiltonian is replaced by the momentum operators] required for the calculations of the Hamiltonian matrix elements when the two interacting carbon atoms are neighbors in the same unit cell.

$(p_{x_{\alpha-\beta}})_{jj'}$	$j'=1$	$j'=2$	$j'=3$	$j'=4$
$j=1$	$P_{x,ss}$	$-P_{x,sp}\cos(\frac{\pi}{6})$	$-P_{x,sp}\cos(\frac{\pi}{3})$	0
$j=2$	$P_{x,sp}\cos(\frac{\pi}{6})$	$P_{x,\sigma}\cos^2(\frac{\pi}{6})-P_{x,\pi}\sin^2(\frac{\pi}{6})$	$(P_{x,\sigma}+P_{x,\pi})\cos(\frac{\pi}{3})\cos(\frac{\pi}{6})$	0
$j=3$	$-P_{x,sp}\cos(\frac{\pi}{3})$	$-(P_{x,\sigma}+P_{x,\pi})\cos(\frac{\pi}{6})\cos(\frac{\pi}{3})$	$-P_{x,\sigma}\cos^2(\frac{\pi}{3})+P_{x,\pi}\sin^2(\frac{\pi}{3})$	0
$j=4$	0	0	0	$P_{x,z}$
$(p_{y_{\alpha-\beta}})_{jj'}$	$j'=1$	$j'=2$	$j'=3$	$j'=4$
$j=1$	0	$P_{y,sp}\sin(\frac{\pi}{6})$	$-P_{y,sp}\sin(\frac{\pi}{3})$	0
$j=2$	$P_{y,sp}\sin(\frac{\pi}{6})$	0	$P_{y,\pi}$	0
$j=3$	$P_{y,sp}\sin(\frac{\pi}{3})$	$P_{y,\pi}$	0	0
$j=4$	0	0	0	0

TABLE V. The matrix elements of the $\hat{P}_{x_{\alpha-\beta}}$ and $\hat{P}_{y_{\alpha-\beta}}$ momentum operators in the bond-dependent coordinates [as enter into Eq. (A8), when the Hamiltonian is replaced by the momentum operators] required for the calculations of the Hamiltonian matrix elements when the two interacting carbon atoms are neighbors but in adjacent unit cells.

$(P_{x_{\alpha-\beta}})_{jj'}$	$j'=1$	$j'=2$	$j'=3$	$j'=4$
$j=1$	$P_{x,ss}$	0	$P_{x,sp}$	0
$j=2$	0	$-P_{x,\pi}$	0	0
$j=3$	$P_{x,sp}$	0	$-P_{x,\sigma}$	0
$j=4$	0	0	0	$P_{x,z}$
$(P_{y_{\alpha-\beta}})_{jj'}$	$j'=1$	$j'=2$	$j'=3$	$j'=4$
$j=1$	0	$-P_{y,sp}$	0	0
$j=2$	$-P_{y,sp}$	0	$P_{y,\pi}$	0
$j=3$	0	$P_{y,\pi}$	0	0
$j=4$	0	0	0	0

- *Present address: Theoretische Chemie, Physikalisch-Chemisches Institut, Universität Heidelberg, Im Neuenheimer Feld 229, D-69120 Heidelberg, Germany.
- ¹P. Salières, A. L'Huillier, P. Antoine, and M. Lewenstein, *Adv. At. Mol. Phys.* **4**, 83 (1999); T. Brabec and F. Krausz, *Rev. Mod. Phys.* **72**, 545 (2000).
- ²R. Haight and D.R. Peale, *Phys. Rev. Lett.* **70**, 3979 (1993).
- ³W. Theobald, R. Häbner, C. Wülker, and R. Sauerbrey, *Phys. Rev. Lett.* **77**, 298 (1996).
- ⁴M. Gisselbrecht, D. Descamps, C. Lyngå, A. L'Huillier, C.-G. Wahlström, and M. Meyer, *Phys. Rev. Lett.* **82**, 4607 (1999).
- ⁵S. Cavalieri, R. Eramo, M. Materazzi, C. Corsi, and M. Bellini, *Phys. Rev. Lett.* **89**, 133002 (2002).
- ⁶Y.R. Shen *The Principal of Nonlinear Optics* (Wiley, New York, 1984).
- ⁷N. Ben-Tal, N. Moiseyev, and A. Beswick, *J. Phys. B* **26**, 3017 (1993).
- ⁸O.E. Alon, V. Averbukh, and N. Moiseyev, *Phys. Rev. Lett.* **80**, 3743 (1998).
- ⁹V. Averbukh, O.E. Alon, and N. Moiseyev, *Phys. Rev. A* **64**, 033411 (2001).
- ¹⁰F. Ceccherini, D. Bauer, and F. Cornolti, *J. Phys. B* **34**, 5017 (2001).
- ¹¹F. Ceccherini and D. Bauer, *Phys. Rev. A* **64**, 033423 (2001).
- ¹²P. Ždánková, V. Averbukh, and N. Moiseyev, *J. Chem. Phys.* **118**, 8726 (2003).
- ¹³O.E. Alon, V. Averbukh, and N. Moiseyev, *Phys. Rev. Lett.* **85**, 5218 (2000).
- ¹⁴R. Velotta, N. Hay, M.B. Mason, M. Castillejo, and J.P. Marangos, *Phys. Rev. Lett.* **87**, 183901 (2001).
- ¹⁵Gy. Farkas, Cs. Tóth, S.D. Moustazis, N.A. Papadogiannis, and C. Fotakis, *Phys. Rev. A* **46**, R3605 (1992).
- ¹⁶D. von der Linde, T. Engers, G. Jenke, P. Agostini, G. Grillon, E. Nibbering, A. Mysyrowicz, and A. Antonetti, *Phys. Rev. A* **52**, R25 (1995).
- ¹⁷P.A. Norreys, M. Zepf, S. Moustazis, A.P. Fewes, J. Zhang, P. Lee, M. Bakarezos, C.N. Danson, A. Dyson, P. Gibbon, P. Loukakos, D. Neely, F.N. Walsh, J.S. Wark, and A.E. Dangor, *Phys. Rev. Lett.* **76**, 1832 (1996).
- ¹⁸I. Watts, M. Zepf, E.L. Clark, M. Tatarakis, K. Krushelnick, A.E. Dangor, R.M. Allott, R.J. Clarke, D. Neely, and P.A. Norreys, *Phys. Rev. Lett.* **88**, 155001 (2002).
- ¹⁹L. Plaja and L. Roso-Franco, *Phys. Rev. B* **45**, 8334 (1992).
- ²⁰F.H.M. Faisal and J.Z. Kamiński, *Phys. Rev. A* **54**, R1769 (1996); **56**, 748 (1997).
- ²¹Y.-S. Lee, M.H. Anderson, and M.C. Downer, *Opt. Lett.* **22**, 973 (1997); Y.-S. Lee and M.C. Downer, *ibid.* **23**, 918 (1998).
- ²²C. Stanciu, R. Ehlich, V. Petrov, O. Steinkellner, J. Herrmann, I.V. Hertel, G.Ya. Slepyan, A.A. Khrtchinski, S.A. Maksimenko, F. Rotermund, E.E.B. Campbell, and F. Rohmund, *Appl. Phys. Lett.* **81**, 4064 (2002).
- ²³M. Lenzner, J. Kruger, S. Sartania, Z. Cheng, Ch. Spielmann, G. Mourou, W. Kautek, and F. Krausz, *Phys. Rev. Lett.* **80**, 4076 (1998).
- ²⁴H.O. Jeschke, M.E. Garcia, and K.H. Bennemann, *Phys. Rev. Lett.* **87**, 015003 (2001).
- ²⁵S. Hüller and J. Meyer-ter-Vehn, *Phys. Rev. A* **48**, 3906 (1993).
- ²⁶M. Holthaus and D.W. Hone, *Phys. Rev. B* **49**, 16 605 (1994).
- ²⁷K.A. Pronin, A.D. Bandrauk, and A.A. Ovchinnikov, *Phys. Rev. B* **50**, 3473 (1994).
- ²⁸G.Ya. Slepyan, S.A. Maksimenko, V.P. Kalosha, J. Herrmann, E.E.B. Campbell, and I.V. Hertel, *Phys. Rev. A* **60**, R777 (1999); G.Ya. Slepyan, S.A. Maksimenko, V.P. Kalosha, A.V. Gusakov, and J. Herrmann, *ibid.* **63**, 053808 (2001).
- ²⁹Yang and Chen, *J. Phys. B* **35**, 4759 (2002).
- ³⁰R. Saito, G. Dresselhaus, and M.S. Dresselhaus, *Physical Properties of Carbon Nanotubes* (Imperial College Press, London, 1998).
- ³¹J.H. Shirley, *Phys. Rev.* **138**, B979 (1965).
- ³²F.H.M. Faisal, *Theory of Multiphoton Processes* (Plenum, New York, 1987).
- ³³W.-K. Shih and Q. Niu, *Phys. Rev. B* **50**, 11902 (1994).
- ³⁴D.F. Martinez, L.E. Reichl, and G.A. Luna-Acosta, *Phys. Rev. B* **66**, 174306 (2002).
- ³⁵U. Peskin and N. Moiseyev, *J. Chem. Phys.* **99**, 4590 (1993).
- ³⁶N. Moiseyev, *Comments At. Mol. Phys.* **31**, 87 (1995).
- ³⁷O.E. Alon, *Phys. Rev. A* **66**, 013414 (2002).

- ³⁸A.L. Altman, *Induced Representations in Crystals and Molecules* (Academic Press, London, 1977); V. Heine, *Group Theory in Quantum Mechanics* (Dover, New York, 1993).
- ³⁹P.B. Corkum, Phys. Rev. Lett. **71**, 1994 (1993); K.C. Kulander, K.J. Schafer, and J.L. Krause, in *Super-Intense Laser-Atom Physics*, Vol. 316 of NATO Advanced Study Institute, Series B: ■, edited by B. Pirax, A. L'Huillier, and K. Rzażewski, (Plenum Press, New-York, 1993), p. 95. M. Lewenstein, Ph. Balcou, M.Yu. Ivanov, A. L'Huillier, and P.B. Corkum, Phys. Rev. A **49**, 2117 (1994).
- ⁴⁰M.Yu. Ivanov and P.B. Corkum, Phys. Rev. A **48**, 580 (1993).
- ⁴¹Z. Chang, A. Rundquist, H. Wang, M.M. Murnane, and H.C. Kapteyn, Phys. Rev. Lett. **79**, 2967 (1997).
- ⁴²J.C. Slater, *Quantum Theory of Atomic Structure Vol. 1, International Series in Pure and Applied Physics*, (McGraw-Hill, New York, 1960).